**ROYAL SOCIETY OF CHEMISTRY**

## PAPER

Check for updates

# DFT study of the moiré pattern of FeO monolayer on Au(111)†

Eleonora Ascrizzi, [ID] [a] Jacek Goniakowski,[b] Jijin Yang,[c] Stefano Agnoli [ID] [c] and Anna Maria Ferrari [ID] *[a]

Metal oxides are a class of material of particular interest for catalytic purposes. Among them the iron oxide as a monolayer supported on gold, FeO/Au, stands out for its capability to promote the CO oxidation and the dissociation of $O_2$ and $H_2$. In this work, we use density functional theory calculations to characterize interfacial properties of this heterostructure. We consider a FeO/Au realistic model system, managing to reproduce the moiré pattern experimentally found. Specific features of the high-symmetry domains of the moiré are identified, providing a robust ground for establishing a structure–activity relationship and guessing how the surface would behave in catalytic conditions. We also describe a strategy to model smaller systems representative of each high-symmetry domains of the moiré, which will be useful in the future to model catalytic reaction mechanisms.

## 1 Introduction

Metal oxides are a class of materials extensively studied for the crucial role they can play with respect to the transition from fossil to renewable energy sources.[1] For example, they can be used as catalysts for the electrochemical or photoelectrochemical water splitting reaction, allowing to obtain hydrogen from sunlight.[2,3] In order to be used in a world-wide scale, a catalyst for these reactions should be not too expensive, earth-abundant and have a low environmental impact: these reasons have guided the research interest towards the exploitation of iron oxides, which proved themselves suitable for these tasks in several occasions.[4–6]

In recent years 2D materials have gained attention because of their high surface area and the accessibility of catalytic sites. Furthermore, thin films possess properties that differ from the bulk materials of origin and these could be exploited to obtain increased catalytic activities.[7] Among iron oxides materials, FeO as a monolayer supported on Pt stands out to be a suitable catalyst for the CO oxidation.[8–10] Given these remarkable results, it would be interesting to see how catalytic properties

can be modified by changing the substrate, for example from Pt to Au which is expected to be a less interacting substrate.[11]

The FeO/Au system has been studied before,[11–15] but not to the same extent as the FeO/Pt one[10,16–23] and so a complete description of the FeO interaction with Au is still to be reached. It is known that FeO and Au give origin to a moiré pattern characterized by the presence of three high-symmetry domains (fcc, hcp and top), as happens for the similar systems FeO/Pt,[24,25] FeO/Pd[26] and FeO/Ag,[27] with a periodicity of *circa* 30 Å.[13–15] Experimentally, the FeO$_x$/Au system was found able to promote CO oxidation and dissociation of $O_2$ and $H_2$, confirming its suitability for catalytic purposes.[11,12] Given the complexity of the FeO$_x$/Au system, only few computational studies have been carried out to rationalize experimental results: Jiang *et al.*[14] and Yu *et al.*[12] performed DFT calculations to shed light on the FeO growth mechanism on Au and on the phase transitions that the system can experience during the interaction with CO, respectively.

Beyond results already reported in the literature, in this paper we aim to acquire precise knowledge of the atomic and electronic structures of the FeO monolayer and of its inter-action with the Au substrate. The focus of this work is to identify specific features that are peculiar of each high-symmetry domain: surface electrostatic potential and work function, local film rumpling, interface distance and charge transfer, which may further determine their different behavior towards water and hydrogen molecules, as it is already known in the FeO/Pt system.[11,16] In this way, the precise characteriza-tion of the three high-symmetry domains of the FeO/Au system provides a robust ground for establishing a structure–activity relationship and guessing how the surface would behave in catalytic conditions. To do so, we simulate an entire FeO/Au

[a] *Dipartimento di Chimica, Università di Torino, via Pietro Giuria 5, I-10125 Turin, Italy. E-mail: anna.ferrari@unito.it*

[b] *CNRS, Sorbonne Université, Institut des NanoSciences de Paris, UMR 7588, 4 Place Jussieu, F-75005 Paris, France*

[c] *Department of Chemical Sciences, University of Padua, via Francesco Marzolo, 1, Padua 35131, Italy*

This journal is © the Owner Societies 2024

*Phys. Chem. Chem. Phys.*, 2024, **26**, 20103–20111 | **20103**

moiré superstructure through DFT+$U$ calculations and, because of its challenging size, we construct a set of suitable smaller models representing the three high-symmetry domains of the moiré in a more affordable way. To validate our model we also experimentally acquire STM images of the FeO/Au system. In particular, in Section 2.1 the experimental method is presented, in Section 2.2 the computational settings used in this work are described as well as the structural models considered, in Section 3 the results are presented and discussed. In Section 3.1 experimentally acquired STM images are presented and described. In Section 3.2 the simulated moiré structure is introduced, characterized and compared with experimental data and literature studies. In Section 3.3 the three high-symmetry domains are modelled in more details with three individual small cells.

## 2 Experimental and computational method

### 2.1 Experimental detail

A Au(111) single crystal was firstly cleaned by repeated cycles of $Ar^{+}$ sputtering (1.5 keV) at room temperature and then annealed at 800 K under ultra-high vacuum conditions for 60 minutes to recover crystallinity. On this surface, a Fe metal film was deposited by physical vapor deposition (PVD), *i.e.* by evaporating iron atoms with an e-beam evaporator at room temperature. The PVD apparatus consists of a custom modified VG Escalab MK II operating at a base pressure of $10^{-10}$ mbar equipped with an e-beam Fe evaporator (EBE-4 Specs GmbH). After the deposition of a submonolayer quantity of iron the sample was annealed at approximately 815 K in an oxygen atmosphere of $5 \times 10^{-7}$ mbar for 20 minutes resulting in the formation of a FeO wetting layer as confirmed by low energy electron diffraction and X-ray photoemission spectroscopy. The STM data were acquired in constant current mode, with a SPM Aarhus (Specs) instruments at room temperature using a kolibri sensor with chemically etched tungsten tips. The STM topographies were analysed with the WSxM software.[28]

### 2.2 Computational detail and model construction

Calculations for the FeO/Au system were carried out thanks to the Vienna *ab initio* Simulation package (VASP).[29–31] The DFT+$U$ approach was chosen to overcome the intrinsic limitation of the method in describing transition metals centers with localized states. This approach allows to obtain reliable band gap values preventing unphysical overlap between occupied and unoccupied bands and a better agreement between computed redox potentials, energy of oxidation and magnetic moments of Fe cations with respect to experiments.[32,33] For the Fe atoms the Dudarev approach[34] has been adopted with $U_{Fe} - J_{Fe} = 3$ eV. The recommended projector augmented wave (PAW) potentials have been used for all atoms, with a kinetic energy cutoff of 400 eV. Spin–orbit coupling (SOC) is not included in calculations. While SOC has a considerable effect on Au band structure, these modifications around the Fermi energy are negligible and so the reactivity and STM images of the Au layer

and the FeO/Au interface (which are the focus of this work) would not change dramatically if SOC was included.[35,36] PBEsol has been adopted as functional, given its suitability in describing solid interfaces and its improved capability in computing more accurate lattice constants.[37] This is a crucial point as the known overestimation of lattice constants by many other GGA functionals would modify the overall coincidence of FeO on Au and the resulting moiré superstructure. With PBEsol functional 4.08 Å was obtained as bulk gold lattice parameter, as experimentally found.[38]

A layer of FeO(111) is put above three layers of Au(111), with two lower layers of Au kept fixed at bulk positions during the structural optimization procedure. The same procedure has been previously successfully applied for the description of FeO/Au and FeO/Pt moiré superstructures.[12,16] Some tests have been performed to assure that three layers of Au are enough to correctly describe the FeO/Au interface, results are collected in Table S1 and Fig. S1 of the ESI.† A vacuum layer of 15 Å has been inserted in between the slabs, with the dipole correction along the non-periodic direction. The resulting structure is shown in Fig. 1 and is characterized by a periodicity of 32 Å, with an angle between FeO and the Au substrate lattices of 9°, in agreement with what was experimentally found.[15] The in plane lattice parameter of Au(111) is 2.88 Å, whereas the lattice parameter of the FeO(111) fully relaxed monolayer is 3.22 Å. The lattice mismatch for the FeO monolayer in the FeO/Au moiré model is about 2% along both the $a$ and $b$ directions. Given the large unit cell considered, consisting of 578 atoms, the Brillouin zone has been sampled at the $\Gamma$ point only. The row-wise antiferromagnetic order has already proven to be the most stable collinear magnetic setting for FeO/Pt[21] so we adopted it for FeO/Au. In the moiré superstructure studied in this work an odd number of iron atoms (103) is present and so
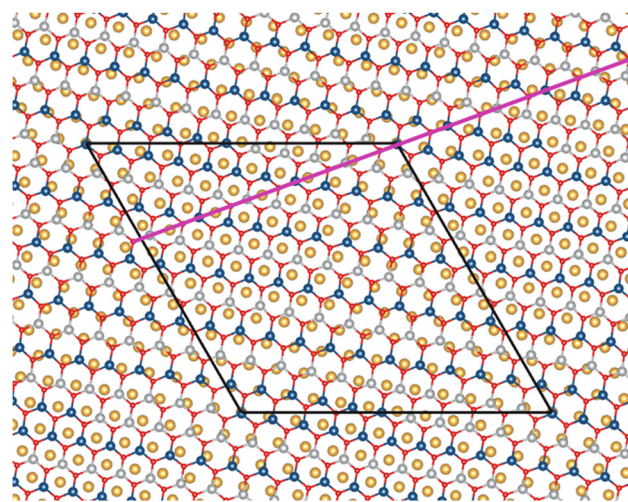


**Fig. 1** Geometry of the FeO/Au moiré superstructure, with only the first gold layer visible for sake of clarity. Red spheres represent oxygen atoms, yellow spheres gold atoms. Grey and blue spheres represent iron atoms with opposite magnetic moment orientation. Black solid line delimits the cell considered for calculations. The plane highlighted in magenta is the one selected for the plots presented in Fig. 5, 7 and 9.

**20104** | *Phys. Chem. Chem. Phys.*, 2024, **26**, 20103–20111

This journal is © the Owner Societies 2024

a magnetic defect, namely a small ferromagnetic zone, can be found in correspondence to the top domain, as already done by Merte et al.[16] for FeO/Pt.

Bader charges analysis has been performed as implemented in the VASP code[39] and STM images have been computed in the framework of the Tersoff–Hamann approximation.[40]

Three high-symmetry domains can be identified in this moiré superstructure: fcc, hcp and top. In the fcc domain both O and Fe atoms are on top of hollow sites of the Au substrate, in hcp O atoms sit atop of Au atoms of the substrate while Fe atoms are on hollow sites and in the top domain the reverse is true, with Fe atoms atop of Au and O atoms on hollow sites. In order to acquire specific data on the three high-symmetry domains of the moiré and have access to local information, three smaller models have been built, one for each domain. Similar models, consisting of a $2 \times 2$ cell of FeO(111) on a $2 \times 2$ cell of Pt(111) have already been used to represent the high-symmetry domains of the FeO/Pt moiré superstructure.[10,17] In this work we go beyond this approximation by adapting the in-plane lattice parameter in the three $2 \times 2$ models, as to reproduce its substantial changes when passing from fcc to hcp and to top domains. More precisely, the mean lattice parameter found for each domain of the moiré, Section 3.2, was then used to build the small models. As in simulation of the full moiré superstructure, also in small models three layers of gold were considered, the lower two fixed. In these models FeO and Au are commensurate to keep the local symmetry: $x$ and $y$ coordinates of Fe atoms are fixed and the substrate is laterally expanded to match the FeO lattice parameter. The optimal Au interplanar spacing has been tuned by relaxing bulk gold for each in-plane lattice parameter considered.

# 3 Results and discussions

## 3.1 STM measurement

A typical STM topography is reported in Fig. 2, which shows the Au(111) substrate fully covered by a monolayer FeO film. On a large scale, it is possible to distinguish a hexagonal modulation of the film corrugation ($\approx 50$ pm) with a pitch of about 3.1 nm,

i.e. the so called moiré superstructure, whereas on a smaller scale also the surface unit cell of the FeO(111) structure becomes apparent, consisting of a hexagonal pattern with a spacing of 3.0 Å. As thoroughly reported in the previous literature,[11–14] the long range modulation of the STM contrast of the moiré superstructure is strongly dependent on the tip conditions (i.e. shape and possible presence of adsorbates) and tunneling parameters (i.e. bias and current).

As a matter of fact, Fig. 3 shows that when the tunneling bias is switched from 0.6 V (empty states, bottom part of the image) to −0.6 V (filled states), a clear change of the topographic contrast takes place, and the moiré, which before was visible as an array of bright dots, is seen as dark round regions separated by brighter edges.

## 3.2 The moire model

The moiré superstructure of FeO/Au depicted in Fig. 1 has been characterised by means of local Fe–Fe distance $l$ (which gives an estimation of the local lattice parameter), film rumpling $\Delta z_{Fe–O} = z_O − z_{Fe}$, interface distance $\Delta z_{FeO–Au} = z_{Fe} + z_O)/2 −z_{Au}$, Fe–O distance $d_{Fe–O}$, atomic charges $q$ and Fe magnetic moment $\mu$. The results collected in Table 1 correspond to averages over the central atom of each high-symmetry domain and its six closest Fe, O and Au neighbors (see Fig. 4).

As expected for metal oxide monolayers deposited on a transition metal substrate, the FeO film on Au is characterized by a significant rumpling with oxygen atoms relaxing outwards.[41] However, the three domains are quite different from each other as regards the lattice parameter, rumpling and interface distance, while the Fe–O distance, atomic charges and magnetic moments remain almost the same. In particular, the fcc domain stands out to be the one with the smallest $l$, the highest $\Delta z_{Fe–O}$ and the lowest $\Delta z_{FeO–Au}$. In contrast, the top one is the one with the largest $l$, the lowest $\Delta z_{Fe–O}$ and the largest $\Delta z_{FeO–Au}$. Finally, the hcp domain displays intermediate
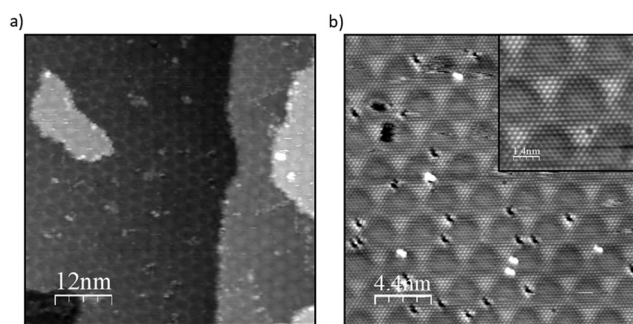


**Fig. 2** STM image at low (a) and high (b) magnification of one monolayer of FeO deposited on the Au(111) surface. The inset in (b) shows a further zoom in on the FeO moiré superstructure. Tunneling parameters: (a) (−1.4 V, 1.5 nA) (b) (−0.9 V, 1 nA). The scale bar is reported on the bottom left corner of the images.
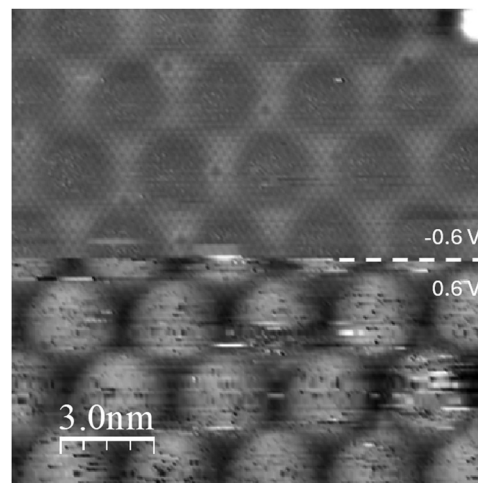


**Fig. 3** STM image of the FeO/Au(111) surface: during the acquisition at the point indicated by the white dashed line the tunneling bias was switched from +0.6 V (bottom part) to −0.6 V (upper part). Tunneling current 1 nA, scale bar on the bottom left of the image.

This journal is © the Owner Societies 2024

Phys. Chem. Chem. Phys., 2024, **26**, 20103–20111 | **20105**

**Table 1** Properties of the three different high-symmetry domains of the FeO/Au moiré superstructure. The lattice parameter $l$ (Fe–Fe distance), the film rumpling $\Delta z_{\text{Fe–O}}$ (computed as $z_O - z_{Fe}$), interface distance $\Delta z_{\text{FeO–Au}}$ (height difference between FeO and the first layer Au, computed as $(z_{Fe} + z_O)/2 - z_{Au}$), Fe–O distance $d_{\text{Fe–O}}$, Bader charges $q_{\text{Fe,O}}$ and iron magnetic moments $\mu_{\text{Fe}}$ are to be intended as mediated for the atoms at the center of each domain (see Fig. 4)

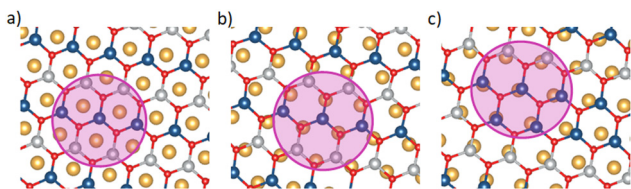| Domain | $l$ [Å] | $\Delta z_{\text{Fe–O}}$ [Å] | $\Delta z_{\text{FeO–Au}}$ [Å] | $d_{\text{Fe–O}}$ [Å] | $q_{\text{Fe}}$ [e] | $q_O$ [e] | $\mu_{\text{Fe}}$ [$\mu_B$] |
|---|---|---|---|---|---|---|---|
| fcc | 3.06 | 0.63 | 2.52 | 1.89 | 1.32 | −1.04 | ±3.73 |
| hcp | 3.21 | 0.40 | 2.69 | 1.90 | 1.29 | −1.12 | ±3.69 |
| top | 3.23 | 0.39 | 2.85 | 1.90 | 1.31 | −1.13 | ±3.73 |



**Fig. 4** The three high-symmetry domains that can be found in the FeO/Au moiré: (a) fcc, (b) hcp, (c) top, with only the first gold layer visible for sake of clarity. Red spheres represent oxygen atoms, yellow spheres gold atoms. Grey and blue spheres represent iron atoms with opposite magnetic moment orientation. The magenta circles indicate the central region of each domain and identify the atoms whose properties are collected in Table 1.

properties. These results show that changes of film rumpling accommodate the differences of its lattice parameter, such that Fe–O bond lengths are the same in the three domains. Regarding this aspect of the local film structure, the fcc domain clearly stands out (the smallest $l$, the largest $\Delta z_{\text{Fe–O}}$), while the hcp and top ones appear quite similar to each other, the only parameter discriminating between them is the interface distance $\Delta z_{\text{FeO–Au}}$, see Table 1.

Regarding electronic characteristics, the difference electron density map presented in Fig. 5 highlights electron redistributions that take place upon formation of the FeO/Au interface from unsupported FeO film and the bare Au substrate. The film-substrate interaction alters mainly the Fe $d_{z^2}$ and O $p_z$ orbitals, but modifications appear to be different in the three high-symmetry domains. The Fe $d_{z^2}$ orbitals are systematically depopulated, but the effect is by far the most pronounced in the fcc domain. The modification of O $p_z$ orbitals is relatively weak in the top and hcp domains, while in the fcc one they become

visibly populated. More importantly, Fig. 5 reveals a substantial charge accumulation at the FeO/Au interface, represented by red zones between the oxide film and the metal substrate. It corresponds to an electron transfer from the FeO film into the Au substrate which, based on Au atomic charges, amounts in average to −0.21 e/FeO. Also in this case, this electron transfer is much more pronounced in the fcc domain, where it also associated with the most visible modifications of charge density at Au atoms in the surface plane of gold.

These results show that in the fcc domain, the FeO film interacts most strongly with the Au substrate, whereas in top and hcp ones the interaction is remarkably weaker. The observation is additionally supported by the behaviour of interface distances in the three domains, Table 1. These differences are expected to impact the local film stability, interface charge transfer and work function in the three domains, but it is not possible to quantify these effects from the full moiré superstructure. This topic will be discussed in Section 3.3, in which smaller models representing the three high-symmetry domains are described.

The results presented in Table 1 can be compared with those obtained for similar FeO/Pt and FeO/Pd systems. Some similarities can be observed, as fcc is recognized to be the most stable domain and the one interacting the most strongly with the substrate, while top is the one that interacts to a lesser extent, also in FeO/Pt and FeO/Pd.[19–21,23,26] In particular, as in our study, also in FeO/Pt and FeO/Pd the local lattice parameter $l$ increases from fcc to hcp to top. Nonetheless, $l$ values in FeO/Au are larger than those reported for FeO/Pt and FeO/Pd (*e.g.* fcc/hcp/top computed $l$ is 3.00/3.09/3.18 Å for FeO/Pd,[26] 3.01/3.08/3.15 Å for FeO/Pt,[20,23] while in this work it is 3.06/3.21/3.23 for FeO/Au). This difference can be assigned to the larger lattice parameter of Au (4.08 Å) compared to Pt and Pd (3.92 Å and 3.89 Å respectively), influencing the whole modulation across the moiré. However, the trend of increasing $l$ from fcc to hcp to top is the same in all the considered systems.

Regarding film rumpling, its relative strength is also the same in the three considered systems, with the fcc domain systematically exposing the largest $\Delta z_{\text{Fe–O}}$, followed by the hcp and the top ones.[20,21,23,26] In terms of their values, the $\Delta z_{\text{Fe–O}}$ is systematically smaller in FeO/Au, (computed $\Delta z_{\text{Fe–O}}$ in fcc/hcp/top domains is 0.74/0.64/0.47 Å for FeO/Pd,[26] 0.77/0.71/0.58 Å for FeO/Pt[20] while in this work is 0.63/0.40/0.39 Å for FeO/Au). This is in part due to a smaller mismatch between FeO and Au lattices but, since film rumpling is also induced by an
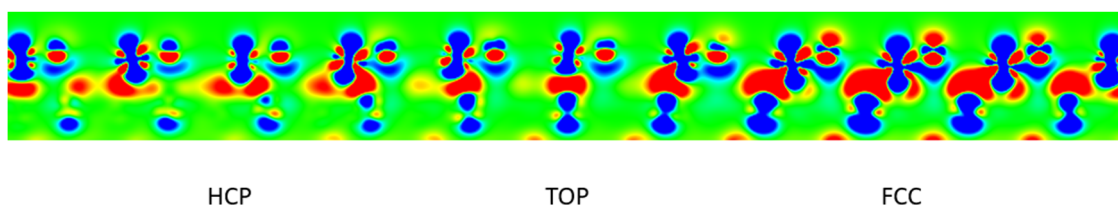


HCP                    TOP                    FCC

**Fig. 5** Difference electron density map between the FeO/Au moiré, the FeO slab and the Au slab, for a plane passing through Fe and O atoms of the three high-symmetry domains. Regions of electron excess and deficiency are depicted in red and blue, respectively. Only the FeO film and the first layer of the Au substrate are shown in this Figure for sake of clarity.

**20106** | *Phys. Chem. Chem. Phys.*, 2024, **26**, 20103–20111

This journal is © the Owner Societies 2024

electrostatic interaction of Fe and O ions with the negatively charged substrate,[41] the smaller $\Delta z_{Fe-O}$ values may also reflect a weaker oxide–metal interaction, accompanied by a smaller interface charge transfer. This observation is supported by the corresponding values of interface distances (fcc/hcp/top computed interface distance is 2.59/2.59/2.70 Å for FeO/Pd,[26] 2.61/2.62/2.77 Å for FeO/Pt,[23] while in this work it is 2.52/2.69/2.85 Å for FeO/Au), which are systematically much longer in the present FeO/Au system. The fcc domain, in which $\Delta z_{FeO-Au}$ is visibly shorter than the corresponding $\Delta z_{FeO-Pt}$ and $\Delta z_{FeO-Pd}$, constitutes an interesting exception. It points again to the particularity of the fcc domain in FeO/Au that, not only structurally stands strongly out with respect to the hcp and top ones, but also does not follow the trends found for the FeO on the Pt and Pd substrates.

We have simulated STM images of the FeO/Au moiré system and results are shown in Fig. 6 and 7. The images in Fig. 6 have been computed at different positive and negative values of bias and taken at heights between 2.5 and 3.5 Å above the FeO layer. The line profiles of the partial charge density (bias +0.3 V) presented in Fig. 7 are plotted for two different density values, in a plane passing through Fe and O atoms in the three high-symmetry domains of the moiré.

Our calculations account fairly well for the overall contrast modulation observed in Fig. 3 and in other experimental studies,[11,14,15] with fcc being the darkest region, top the brightest and hcp the one with an intermediate contrast, regardless the value of bias, Fig. 6. Also the line profiles, Fig. 7, show that the average apparent height is the smallest in the fcc domain and the largest in the top one, roughly following the mean

eometric heights of surface ions in the three domains (the same relative height is found in the FeO/Pt moiré superstructure[20]). Our computed STM images reproduce in a excellent way the experimental STM image reported in Fig. 3 and appear to be sensitive to the applied bias, without unfortunately reproducing the inversion of contrast passing from negative to positive biases. However in the work from Yang *et al.* the top region is found to be the brightest at both negative and positive biases (see Fig. 2 of ref. 15) as in our simulated images.

On the computational side, the accuracy of the theoretical method is limited by the Tersoff–Hamann approximation we are working with.[40] The STM images are obtained by sampling the electron density of the FeO/Au system only, whereas the experimentally measured contrast is driven by the chemical interaction between surface atoms and the specific tip state,[20] which is completely neglected in this computational framework. This dependency of the contrast from the tip leads to a great variability also in experimentally acquired STM images, emphasizing the complexity and sensitivity of the technique. Specific tip states can be considered in first principle calculations in the framework of the Bardeen's method[42] or Chen's derivative method,[43] explicitly modelling the atoms of the tip and overcoming the limitation of the Tersoff–Hamann approximation. These approaches are however more suited for the study of a localised point of interest rather than for obtaining the STM image of a whole surface as we desire for the FeO/Au moiré superstructure.[44,45] Considering the large dimension of our cell and the diverse morphology it presents along the lattice parameter, the STM simulation would require a complex modelling of the substrate/tip interaction, which which would be difficult to construct and would exceed our computational power.

Interestingly, the origin of the calculated atomically-resolved contrast is different in the three domains as depicted in Fig. 7. In the fcc one, surface oxygen atoms produce a much more pronounced contrast than the Fe atoms, which is consistent with the large film rumpling and their relative geometric height in this domain. In contrast, in the top domain, the STM contrast is mainly due to surface Fe ions. In this region the geometric effect is less strong (film rumpling is much smaller), such that the electronic effect, associated to a large density of unoccupied Fe states (see Fig. 8), contributes also to the STM contrast. In the hcp domain, the Fe and O atoms display a similar apparent height deriving from the partial charge density: both of them should be visible in STM images. No assignment of the atomically-resolved contrast to particular surface ions was proposed in other experimental studies.[11,14,15]

Comparing with the similar and more studied FeO/Pt system, considering both experimental and theoretical studies, we can see that the modulation across the moiré is essentially the same.[10,16,19,20,23] On FeO/Pt an unambiguous determination of the three different domains of the moiré was achieved by Merte *et al.*, who have inserted defects in the different domains in order to identify them in STM images.[19,20] They found that in their and in most studies, the top domain is the brightest at positive and slightly negative biases, while it becomes dark at negative bias values.[20] It is more difficult to discriminate in
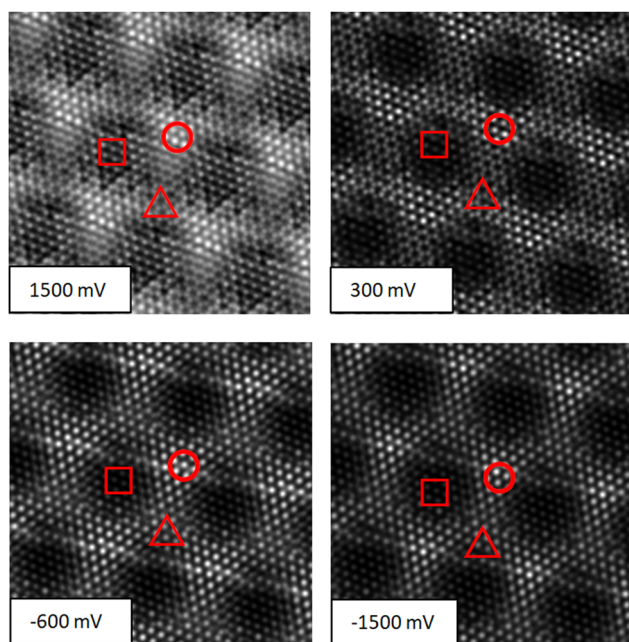


**Fig. 6** STM images for the FeO/Au moiré superstructure computed in this work at different biases. Symbols mark the three high-symmetry domains: □ fcc, Δ hcp, and ○ top. Computed images are taken at 2.5 Å above the FeO layer.
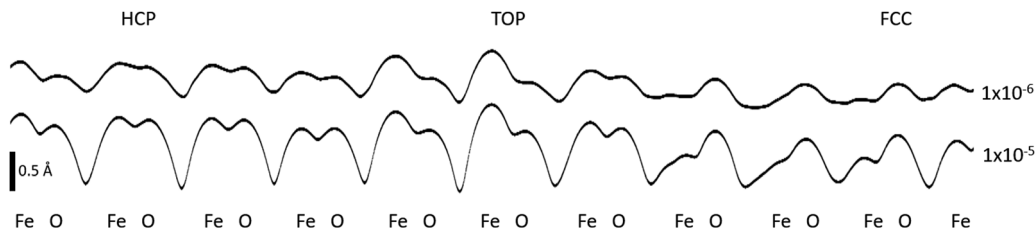
This journal is © the Owner Societies 2024

*Phys. Chem. Chem. Phys.,* 2024, **26**, 20103–20111 | **20107**

**Fig. 7** Line profiles extracted form the moiré STM image at +0.3 V, showing the variation across the three high-symmetry domains of the moiré. Isolines are taken at $10^{-5}$ and $10^{-6}$ e/Å$^3$.
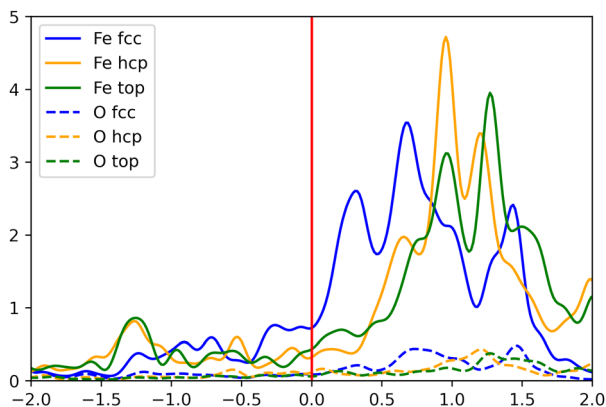


**Fig. 8** PDOS (projected density of states) of the central atoms at the three symmetry regions: blue line for fcc, green line for top and yellow line for hcp. Solid lines represent Fe PDOS, dashed lines O PDOS. Alpha and beta states have been summed in this plot. The Fermi energy ($E_f$) is marked with a red line.

between the hcp and fcc domains: fcc has the lowest work function and so it is often recognized to be the darkest region, but it is not easy to differentiate its contrast from the one of hcp, especially at low bias values.[19,20] Furthermore, FeO/Pt STM images were recognized to be "mixed", meaning that atomic contrast in STM images corresponds to either surface O or Fe atoms, depending on the high-symmetry domain. In particular protrusions due to Fe atoms were found in the top domain, to O atoms in the fcc domain, while in the hcp one a nearly equal tip height was found over surface O and Fe atoms.[20]

All these characteristics are consistent with our present results on FeO/Au, thus validating our approach. The main difference is that the calculated STM contrast for FeO/Au is the same for every bias value. Aiming not only to rationalize the experimental STM images, but also to enquire on the origin of the contrast modulation, the electrostatic potential above the FeO/Au surface has been computed, and it is shown in a plane passing through the three high-symmetry domains of the moiré in Fig. 9.

The fcc domain is characterized by a large zone of surface electrostatic potential that is strongly repulsive for electrons (red), while the top one produces an overall attractive electrostatic effect (blue). This makes electron tunneling more difficult in the fcc domain (where the local work function is expected to be the largest) than in the top one (where it is expected to be the

smallest). Since a larger work function generally results in a lower tunneling current,[46] the modulation of the surface electrostatic potential could be held responsible for the overall modulation of the STM contrast, and the dark (bright) appearance of the fcc (top) domains in Fig. 6.

### 3.3 2 × 2 models

Computational results for the full moiré superstructure do not give access some of the local properties such as the work function $\Phi$, the interface charge transfer CT and the adhesion energy $E_{ad}$ between the FeO film and the Au substrate. All of these features are important not only to further interpret the STM contrast but also for a first assessment of reactivity differences in the three high-symmetry domains. Small 2 × 2 models of the fcc, hcp and top domains have been built, with in-plane lattice parameters $l$ estimated at the three high-symmetry domains of the moiré superstructure (Table 1). The structural and electronic characteristics are reported in Table 2.

Even at this level of approximation the resemblance with data in Table 1 is remarkable, since not only all the trends are correctly reproduced, but also the computed values of $\Delta z_{\text{Fe–O}}$, $\Delta z_{\text{FeO–Au}}$, $d_{\text{FeO}}$, $q$ and $\mu$ are quite similar to what was found in the moiré superstructure, assuring that these small models can indeed convincingly represent the three domains. As described in Table 1 for the full moiré superstructure, also in these smaller models the two principal features that discriminate the three domains are $\Delta z_{\text{Fe–O}}$ and $\Delta z_{\text{FeO–Au}}$, while $d_{\text{Fe–O}}$, $q$ and $\mu$ are the same in all the high-symmetry domains. The additional features presented in Table 2 are $E_{ad}$, CT and $\Phi$. CT has a negative sign as expected for metal oxide monolayers deposited on a transition metal support.[41] Because of high electronegativity of the Pt substrate, electrons move from cations of the oxide film to the substrate and the overall structural response to this interfacial charge transfer is the rumpling of FeO, with oxygens relaxing outwards. As a consequence, the strengths of film rumpling and interface charge transfer are correlated, with their maximal values found in the fcc domain. The most negative $E_{ad}$ found in the fcc domain confirms that there the film-substrate interaction is the strongest. This fact is additionally corroborated by the the smallest value of $\Delta z_{\text{FeO–Au}}$ and the shortest $l$. In contrast, $E_{ad}$ is the least negative in the top domain. This confirms the weak interaction with the substrate, consistent with the smallest CT and the largest $\Delta z_{\text{FeO–Au}}$. Finally, the value $\Delta\Phi$ reported in Table 2 represents the work function difference between the FeO/Au system and the bare
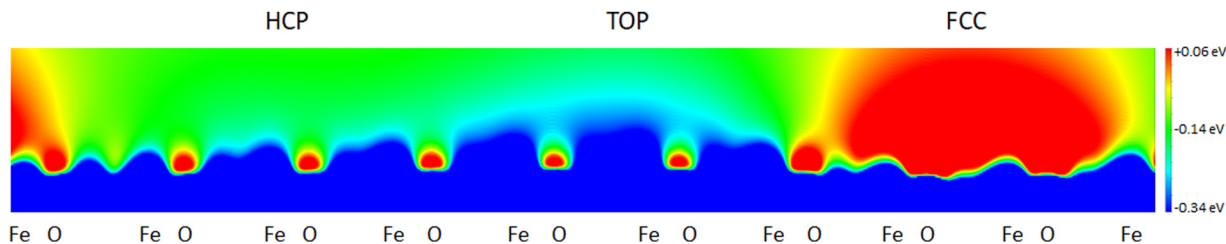
**20108** | *Phys. Chem. Chem. Phys.*, 2024, **26**, 20103–20111

This journal is © the Owner Societies 2024

**Fig. 9** Electrostatic potential of the FeO/Au surface plotted on a plane passing through Fe and O atoms in the three high-symmetry regions of the moiré.

**Table 2** Properties of the three high-symmetry domains, here modelled as (2 × 2) cells with a lattice parameter of 3.06 Å for fcc, 3.21 Å for hcp and 3.23 Å for top. $l$ is lattice parameter (Fe–Fe distance), $\Delta z_{Fe-O}$ is the rumpling (computed as $z_O - z_{Fe}$), $\Delta z_{FeO-Au}$ is the interface distance (height difference between FeO and the first layer Au, computed as $(z_{Fe} + z_O/2 - z_{Au})$, $d_{Fe-O}$ is the Fe–O distance, $q_{Fe,O}$ is the Bader charge and $\mu_{Fe}$ is the iron magnetic moment. Adhesion energy ($E_{ad}$) and interface charge transfer towards the substrate (CT) are given per FeO unit. $\Delta\Phi$ is the difference between the work function of the FeO/Au system and of the bare Au(111) surface, reported in brackets

| Domain | $l$ [Å] | $\Delta z_{Fe-O}$ [Å] | $\Delta z_{FeO-Au}$ [Å] | $d_{Fe-O}$ [Å] | $q_{Fe}$ [e] | $q_O$ [e] | $\mu_{Fe}$ [$\mu_B$] | $E_{ad}$ [eV] | CT | $\Delta\Phi$ [eV] |
|---|---|---|---|---|---|---|---|---|---|---|
| fcc | 3.06 | 0.68 | 2.48 | 1.87 | +1.31 | −1.03 | ±3.71 | −0.66 | −0.28 | +0.31 (+5.44) |
| hcp | 3.21 | 0.44 | 2.53 | 1.90 | +1.24 | −1.11 | ±3.65 | −0.56 | −0.13 | −0.35 (+5.24) |
| top | 3.23 | 0.32 | 2.80 | 1.89 | +1.27 | −1.14 | ±3.66 | −0.53 | −0.12 | −0.79 (+5.16) |

Au(111) surface, presented in brackets in Table 2. Again, the fcc domain stands out, being the only one with a positive $\Delta\Phi$ value and a $\Phi$ considerably larger than that in the hcp and top domains, suggesting that the dipole moment associated to the film rumpling determines the modulation of the local work function. We notice that the domains with the largest and the smallest work function (fcc and top, respectively), correspond well to those with the most repulsive and attractive surface electrostatic potential in Fig. 9, respectively.

When comparing these results with a previous literature study on small models for the three high symmetry domains of FeO/Pt[21] we can see that also in this case the trends for $l$, $\Delta z_{Fe-O}$, $\Delta z_{FeO-Au}$, $E_{ad}$ and $\Phi$ are the same for the three domains. The one thing that stands out the most when comparing the two works, is that in FeO/Pt the hcp domain has characteristics (such as $\Delta z_{Fe-O}$ and the $\Phi$) which are closer to fcc, while in FeO/Au the hcp domain seems to be more similar to top. Again, as observed for the moiré superstructure, in FeO/Au $\Delta z_{Fe-O}$ for hcp and top is lower with respect to the value computed for FeO/Pt (*i.e.* computed $\Delta z_{Fe-O}$ for FeO/Pt smaller models fcc/hcp/top is 0.68/0.65/0.51 Å,[21] while in this work the computed $\Delta z_{Fe-O}$ for FeO/Au smaller models is 0.68/0.44/0.32 Å). This results also in a lower $\Delta\Phi$ in FeO/Au compared to FeO/Pt (*i.e.* computed $\Delta\Phi$ for FeO/Pt smaller models fcc/hcp/top is +0.49/+0.13/−0.60 eV[21] while in this work the computed $\Delta\Phi$ for FeO/Au smaller models is +0.31/−0.35/−0.79 eV). This behaviour may derive from Au larger parameter with respect to Pt, but also by a lower charge transfer from FeO to Au. This can be true especially at the top and hcp domains, in which a lower charge transfer may be the cause of the lower rumpling and $\Delta\Phi$ found out when comparing FeO/Au to FeO/Pt.

From data collected in Table 2, we can conclude that the fcc domain has the strongest interaction with the substrate and

this determines $\Delta z_{FeO-Au}$ to be the shortest and the CT towards gold to be largest. The $\Delta z_{Fe-O}$ here is the largest because it is a structural response to the interfacial CT.[41] As seen before, the opposite can be said for top, while hcp has intermediate characteristics. These features are different in the three high symmetry domains and are the cause of different $\Phi$ and different contrast in STM.

## 4 Conclusions

In this work we characterized the FeO/Au system, comparing our results to the more studied FeO/Pt and FeO/Pd systems to validate our method. We studied the moiré superstructure as a whole and three smaller models of the three high-symmetry domains in order to acquire specific information. We reproduced experimental STM images, rationalized the origin of their contrast and how it changes with respect to the bias and the tunneling distance. Different specific features identified in the three high-symmetry domains, such as surface electrostatic potential and work function, local film rumpling, interface distance and charge transfer, may suggest different adsorption and reactivity properties across the FeO/Au moiré, as happens for FeO/Pt.[11,16]

In general FeO/Au results to be similar to FeO/Pt and FeO/Pd. Nonetheless, some differences as the lower rumpling, the work function and their correlation with the surface electrostatic potential can be important in determining the surface reactivity towards water and the possible exploitation of this system as a catalyst for the electrochemical water splitting reaction. Further studies are needed to have a better understanding of the reactivity towards water, both from an experimental and computational point of view.
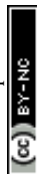
In this work we have proposed a strategy to build smaller models for the three high-symmetry domains, keeping the local characteristics that can be found in the entire structure. This approach could be useful in the future to allow the simulation of different adsorption mechanisms that would be prohibitive considering a system of the size of the entire moiré.

## Author contributions

## Data availability

The authors confirm that the data supporting the findings of this study are available within the article and its ESI.†

## Conflicts of interest

There are no conflicts to declare.

## Acknowledgements

## References

1 I. Concina, Z. H. Ibupoto and A. Vomiero, *Adv. Energy Mater.*, 2017, **7**, 1700706.

2 I. C. Man, H.-Y. Su, F. Calle-Vallejo, H. A. Hansen, J. I. Martínez, N. G. Inoglu, J. Kitchin, T. F. Jaramillo, J. K. Nørskov and J. Rossmeisl, *ChemCatChem*, 2011, **3**, 1159–1165.

3 T. Jafari, E. Moharreri, A. S. Amin, R. Miao, W. Song and S. L. Suib, *Molecules*, 2016, **21**, 900.

4 J.-W. Jang, C. Du, Y. Ye, Y. Lin, X. Yao, J. Thorne, E. Liu, G. McMahon, J. Zhu, A. Javey, J. Guo and D. Wang, *Nat. Commun.*, 2015, **6**, 1–5.

5 J. S. Kang, Y. Noh, J. Kim, H. Choi, T. H. Jeon, D. Ahn, J.-Y. Kim, S.-H. Yu, H. Park, J.-H. Yum, W. Choi, D. C. Dunand, H. Choe and Y.-E. Sung, *Angew. Chem., Int. Ed.*, 2017, **56**, 6583–6588.

6 B. H. R. Suryanto, Y. Wang, R. K. Hocking, W. Adamson and C. Zhao, *Nat. Commun.*, 2019, **10**, 1–10.

7 C. J. Heard, J. Čejka, M. Opanasenko, P. Nachtigall, G. Centi and S. Perathoner, *Adv. Mater.*, 2019, **31**, 1801712.

8 Q. Fu, W.-X. Li, Y. Yao, H. Liu, H.-Y. Su, D. Ma, X.-K. Gu, L. Chen, Z. Wang, H. Zhang, B. Wang and X. Bao, *Science*, 2010, **328**, 1141–1144.

9 Y.-N. Sun, Z.-H. Qin, M. Lewandowski, E. Carrasco, M. Sterrer, S. Shaikhutdinov and H.-J. Freund, *J. Catal.*, 2009, **266**, 359–368.

10 L. Giordano, M. Lewandowski, I. M. N. Groot, Y.-N. Sun, J. Goniakowski, C. Noguera, S. Shaikhutdinov, G. Pacchioni and H.-J. Freund, *J. Phys. Chem. C*, 2010, **114**, 21504–21509.

11 Y. Li, K. C. Adamsen, L. Lammich, J. V. Lauritsen and S. Wendt, *ACS Nano*, 2019, **13**, 11632–11641.

12 L. Yu, Y. Liu, F. Yang, J. Evans, J. A. Rodriguez and P. Liu, *J. Phys. Chem. C*, 2015, **119**, 16614–16622.

13 N. A. Khan and C. Matranga, *Surf. Sci.*, 2008, **602**, 932–942.

14 Y. Jiang, S. Bu, D. Zhou, X. Shi, F. Pan, Q. Ji and T. Niu, *J. Phys. Chem. C*, 2021, **125**, 24755–24763.

15 S. Yang, J. Gou, P. Cheng, L. Chen and K. Wu, *Phys. Rev. Mater.*, 2020, **4**, 074004.

16 L. R. Merte, R. Bechstein, G. Peng, F. Rieboldt, C. A. Farberow, H. Zeuthen, J. Knudsen, E. Lægsgaard, S. Wendt, M. Mavrikakis and F. Besenbacher, *Nat. Commun.*, 2014, **5**, 1–9.

17 F. Ringleb, Y. Fujimori, H.-F. Wang, H. Ariga, E. Carrasco, M. Sterrer, H.-J. Freund, L. Giordano, G. Pacchioni and J. Goniakowski, *J. Phys. Chem. C*, 2011, **115**, 19328–19335.

18 M. Ritter, W. Ranke and W. Weiss, *Phys. Rev. B: Condens. Matter Mater. Phys.*, 1998, **57**, 7240–7251.

19 L. R. Merte, J. Knudsen, L. C. Grabow, R. T. Vang, E. Lægsgaard, M. Mavrikakis and F. Besenbacher, *Surf. Sci.*, 2009, **603**, L15–L18.

20 L. R. Merte, L. C. Grabow, G. Peng, J. Knudsen, H. Zeuthen, W. Kudernatsch, S. Porsgaard, E. Lægsgaard, M. Mavrikakis and F. Besenbacher, *J. Phys. Chem. C*, 2011, **115**, 2089–2099.

21 L. Giordano, G. Pacchioni, J. Goniakowski, N. Nilius, E. D. L. Rienks and H.-J. Freund, *Phys. Rev. B: Condens. Matter Mater. Phys.*, 2007, **76**, 075416.

22 L. Giordano, G. Pacchioni, J. Goniakowski, N. Nilius, E. D. L. Rienks and H.-J. Freund, *Phys. Rev. Lett.*, 2008, **101**, 026102.

23 W. Zhang, Z. Li, Y. Luo and J. Yang, *J. Phys. Chem. C*, 2009, **113**, 8302–8305.

24 W. Weiss and W. Ranke, *Prog. Surf. Sci.*, 2002, **70**, 1–151.

25 Y. J. Kim, C. Westphal, R. X. Ynzunza, H. C. Galloway, M. Salmeron, M. A. Van Hove and C. S. Fadley, *Phys. Rev. B: Condens. Matter Mater. Phys.*, 1997, **55**, R13448.

26 H. Zeuthen, W. Kudernatsch, G. Peng, L. R. Merte, L. K. Ono, L. Lammich, Y. Bai, L. C. Grabow,

**20110** | *Phys. Chem. Chem. Phys.*, 2024, **26**, 20103–20111

This journal is © the Owner Societies 2024

M. Mavrikakis, S. Wendt and F. Besenbacher, *J. Phys. Chem. C*, 2013, **117**, 15155–15163.

27 M. Lewandowski, T. Pabisiak, N. Michalak, Z. Miłosz, V. Babači, Y. Wang, M. Hermanowicz, K. Palotaás, S. Jurga and A. Kiejna, *Nanomaterials*, 2018, **8**, 828.

28 I. Horcas, R. Fernández, J. M. Gómez-Rodríguez, J. Colchero, J. Gómez-Herrero and A. M. Baro, *Rev. Sci. Instrum.*, 2007, **78**(1), 013705.

29 G. Kresse and J. Hafner, *Phys. Rev. B: Condens. Matter Mater. Phys.*, 1993, **47**, 558–561.

30 G. Kresse and J. Furthmüller, *Comput. Mater. Sci.*, 1996, **6**, 15–50.

31 G. Kresse and J. Furthmüller, *Phys. Rev. B: Condens. Matter Mater. Phys.*, 1996, **54**, 11169–11186.

32 M. Shishkin and H. Sato, *J. Chem. Phys.*, 2019, **151**(2), 024102.

33 M. Cococcioni and S. de Gironcoli, *Phys. Rev. B: Condens. Matter Mater. Phys.*, 2005, **71**, 035105.

34 S. L. Dudarev, G. A. Botton, S. Y. Savrasov, C. J. Humphreys and A. P. Sutton, *Phys. Rev. B: Condens. Matter Mater. Phys.*, 1998, **57**, 1505–1509.

35 P. Romaniello and P. L. de Boeij, *J. Chem. Phys.*, 2005, **122**(16), 164303.

36 H. A. Alluhaybi, S. K. Ghoshal, B. O. Alsobhi and W. N. W. Shamsuri, *Comput. Condens. Matter*, 2019, **18**, e00360.

37 J. P. Perdew, A. Ruzsinszky, G. I. Csonka, O. A. Vydrov, G. E. Scuseria, L. A. Constantin, X. Zhou and K. Burke, *Phys. Rev. Lett.*, 2008, **100**, 136406.

38 R. W. G. Wyckoff and R. W. Wyckoff, *Crystal structures*, Interscience publishers, New York, 1963, vol. 1.

39 W. Tang, E. Sanville and G. Henkelman, *J. Phys.: Condens. Matter*, 2009, **21**, 084204.

40 J. Tersoff and D. R. Hamann, *Phys. Rev. B: Condens. Matter Mater. Phys.*, 1985, **31**, 805–813.

41 J. Goniakowski and C. Noguera, *Phys. Rev. B: Condens. Matter Mater. Phys.*, 2009, **79**, 155433.

42 J. Bardeen, *Phys. Rev. Lett.*, 1961, **6**, 57–59.

43 C. J. Chen, *Phys. Rev. B: Condens. Matter Mater. Phys.*, 1990, **42**, 8841–8857.

44 S. Duan, G. Tian and X. Xu, *JACS Au*, 2023, **3**, 86–92.

45 A. Gustafsson and M. Paulsson, *Phys. Rev. B*, 2016, **93**, 115434.

46 G. Binnig, H. Rohrer, Ch Gerber and E. Weibel, *Phys. Rev. Lett.*, 1982, **49**, 57–61.

This journal is © the Owner Societies 2024

*Phys. Chem. Chem. Phys.*, 2024, **26**, 20103–20111 | **20111**